J. Fluid Mech. (2008), *vol.* 599, *pp.* 205–228. © 2008 Cambridge University Press
doi:10.1017/S0022112008000165 Printed in the United Kingdom

Parametrically forced gravity waves in a circular cylinder and finite-time singularity

S. P. DAS AND E. J. HOPFINGER
LEGI/CNRS/UJF, BP 53, 38041 Grenoble Cedex, France
hopfinger@hmg.inpg.fr

(Received 6 June 2007 and in revised form 29 November 2007)

In this paper we present results on parametrically forced gravity waves in a circular cylinder in the limit of large fluid-depth approximation. The phase diagram that shows the forcing-amplitude instability and the wave-breaking thresholds has been determined in the frequency range of existence of the lowest axisymmetric wave mode. The instability is shown to be supercritical for forcing frequencies at and above the natural frequency and subcritical below in a frequency range where the instability and breaking thresholds do not coincide. Above the instability threshold, the growth in wave amplitude is exponential, but with an initial time delay. The wave-amplitude response curve of stationary wave motions exhibits steady-state wave motion, amplitude modulations and bifurcations to other wave modes at frequencies where the parametric instability boundary of the axisymmetric mode overlaps with the neighbouring modes. The amplitude modulations are either on a slow time scale or exhibit period tripling and intermittent period tripling, without wave breaking. In the wave-breaking regime, a finite-time singularity may occur with intense jet formation, a phenomenon demonstrated by others in fluids of high viscosity and large surface tension. Here, this singular behaviour with jet formation is demonstrated for a low viscosity and low kinematic surface tension liquid. The results indicate that the jet is driven by inertial collapse of the cavity created at the wave trough. Therefore, the jet velocity is determined by the wave fluid velocity but depends, in addition, on kinematic surface tension and viscosity as these affect the last stable wave crest shape and the cavity size.

1. Introduction

Parametrically forced surface waves, known as Faraday waves, that are sub-harmonically excited, have been studied extensively (Benjamin & Ursell 1954; Miles & Henderson 1990; Edwards & Fauve 1994; Kumar & Tuckermann 1994). However, far less is known about large-amplitude waves and wave-breaking conditions, especially of parametrically forced gravity waves. Large-amplitude sloshing in containers is encountered in rocket engine fuel tanks and ship tanks. In these applications it is important to be able to predict the liquid behaviour and to evaluate the forces exerted by the sloshing motion on the tank walls as well as the consequences of sloshing and wave breaking on interfacial heat and mass transfer. The wave modes in containers of various geometries can be found in Abramson (1966) and in Ibrahim (2005). Miles (1984) developed a weakly nonlinear theory of wave motions in circular cylinders subjected to horizontal forcing that contains the relevant control parameters and allows the determination of the phase diagram of sloshing. This phase diagram

https://doi.org/10.1017/S0022112008000165 Published online by Cambridge University Press

is in good agreement with experiments (Royon-Lebeaud, Hopfinger & Cartellier 2007). The multimodal theory can cope with fully nonlinear sloshing (excluding wave breaking) and has been successfully applied to rectangular and square-based containers (Faltinsen *et al.* 2000, 2003).

Parametrically forced gravity waves have been investigated mainly near the instability threshold and in the weakly nonlinear regime. Various surface wave modes, tank geometries and depth to radius ratios have been considered (Dodge 1966; Nayfeh 1987; Feng & Sethna 1989; Simonelli & Gollub 1989). Reviews of these studies and of the general, weakly nonlinear theory of parametrically forced surface waves are given in Miles & Henderson (1990) and in Ibrahim (2005). The depth to radius ratio is known to be an important parameter because this determines the nonlinear resonance. Furthermore, a small depth to radius ratio enhances the development of secondary modes. Large-amplitude parametrically forced gravity waves have received less attention. In two dimensions, Jiang, Perlin & Schultz (1998) showed the occurrence of a period tripling event connected with breaking or spilling that is further discussed in Perlin & Schultz (2000). Bredmose *et al.* (2003) conducted experiments in a rectangular tank that showed the existence of tabletop breaking waves. The wave crest of gravity waves is unstable when the wave amplitude has reached a value such that the downward acceleration of the wave crest is equal to or slightly larger than gravity (Taylor 1953). For larger amplitudes free fall of lumps of fluid near the wave crest is, therefore, possible, a phenomenon essential to period tripling and tabletop wave crest formation. Henderson & Miles (1990, hereinafter referred to as HM) determined the parametric instability conditions and the steady-state wave-amplitude response of the axisymmetric wave mode (0,1) in a 'small' circular cylinder; the wave modes (m, n) express m nodal diameters and $n - 1 + \delta_{m0}$ nodal circles with $m = 0, 1, \ldots$ and $n = 1, 2, \ldots$, where δ_{m0} is the Kronecker delta function. Small implies that capillary and viscous effects are significant. For a given container size, this depends, however, on the liquid properties.

In a circular cylinder, axisymmetric wave breaking can be very violent with jet formation. Zeff *et al.* (2000) demonstrated the occurrence of a finite-time singularity with intense jet formation (also referred to as a geyser in the space science literature) in a glycerine–water solution. The large viscosity is said to be necessary for preventing parasitic capillary wave disturbances on the wave surface that reduce the finite-time singularity. In the model of Zeff *et al.* the jet velocity is proportional to the square root of the kinematic surface tension. It is of general interest to verify this model.

In this paper, we present results on parametrically forced gravity waves in circular cylinders of sizes similar to those of HM and to Zeff *et al.* but using, primarily, a fluid with very low kinematic viscosity and kinematic surface tension so that capillary effects and dissipation remain small. In § 3, the essential aspects of the HM theory are presented. Then in § 4, we first compare the experimental phase diagram of forcing amplitude versus wave frequency with the theoretical predictions by HM, taking into account small surface tension and viscosity corrections. This phase diagram is completed by the wave-breaking threshold. The wave-amplitude response curves, obtained for the same frequency domain, exhibit the existence of steady-state wave motion, amplitude modulations and wave breaking. The nature of the parametric instability and the wave amplification are discussed in § 5. The finite-time singularity, associated with breaking of the axisymmetric mode, which leads to intense jet formation, is presented in § 6. In order to determine the possible dependence on surface tension, this jet formation has been investigated in two different sized containers using three different liquids.

https://doi.org/10.1017/S0022112008000165 Published online by Cambridge University Press

2. Experimental conditions

The experiments have been conducted in circular cylindrical plexiglas containers, one of diameter $2R = 50\,\text{mm} \pm 0.03$ and 6 cm deep, and the other of $2R = 100\,\text{mm}$ ± 0.04 and 10 cm deep, mounted on a vertically oscillating vibration exciter, TIRA, type TV 52120 of peak force 200 N. After calibration, the vibration amplitude could be kept within ± 0.30 % of the nominal value and the frequency within 0.02%. Since the vibration is normal to the fluid surface, the waves are sub-harmonically excited. The larger container was constructed in order to clarify the possible dependency of jet formation on kinematic surface tension. The smaller container was filled to a depth $h = 3\,\text{cm}$ with a low viscosity and low surface tension liquid, FC-72, of $\nu = 0.00406\,\text{cm}^2\,\text{s}^{-1}$, $\sigma = 11\,\text{dyn}\,\text{cm}^{-1}$ and $\rho = 1690\,\text{kg}\,\text{m}^{-1}$ at 20 °C. The corresponding Bond number is $Bo = \rho g R^2/\sigma = 942$. The larger container was filled to a depth $h = 6\,\text{cm}$ with FC-72 liquid and also with a glycerine–water solution of $\nu = 2.7\,\text{cm}^2\,\text{s}^{-1}$, $\sigma = 65\,\text{dyn}\,\text{cm}^{-1}$ and $\rho = 1260\,\text{kg}\,\text{m}^{-3}$ at 20 °C. The respective Bond numbers are 3768 for FC-72 and 376 for glycerine–water. Some experiments on jet formation were done with distilled water and with distilled water and 1 % ILFORD ILFOTOL fluid added. Experiments were conducted at room temperature, generally around 20 to 23 °C. In both containers, the fluid depth to radius ratio was $h/R = 1.2$, that is sufficient to satisfy deep-water conditions ($\tanh(k_{01}h) \cong 1$) for the axisymmetric mode (Miles & Henderson 1990). The liquid FC-72 is fully wetting (the contact line is free to move) with a static contact angle close to zero. In the case of water or glycerine–water solution, the contact line is practically fixed (see the Appendix). The container acceleration $a(t) = A\omega_f^2 \sin\omega_f t$, in the experiments is $a(t) \leqslant 6\,\text{m}\,\text{s}^{-2}$ where ω_f is the circular forcing frequency, equal to twice the wave frequency ω, and A is the forcing amplitude.

Measurements were made by visualizations and image analysis only. Generally, a digital camera with an acquisition speed of 60 frames s^{-1} (f.p.s.) was used. Near resonant conditions with high-velocity jet formation, images were also taken with a high-speed camera at 1000 f.p.s.

3. Theoretical concepts

The weakly nonlinear theory of axisymmetric wave motion in a circular cylinder has been developed by HM following Miles (1984). A detailed outline of this theory is given in Ibrahim (2005). The dispersion relation with surface tension added is

$$\omega_{mn}^2 = g k_{mn}\left(1 + \frac{k_{mn}^2\sigma}{g\rho}\right)\tanh(k_{mn}h). \tag{1}$$

The boundary condition on the container wall is $\partial\phi/\partial r|_{r=R} = J'_m(k_{mn}R) = 0$, where ϕ is the velocity potential, which gives for the axisymmetric wave modes, $m = 0$ and $n = 1$ and $n = 2$, $k_{01}R = 3.8317$ and $k_{02}R = 7.0156$. For the asymmetric modes, the dimensionless wavenumbers are: $k_{11}R = 1.841$, $k_{21}R = 3.054$, $k_{31}R = 4.201$, $k_{41}R = 5.318$, $k_{12}R = 5.331$. The corresponding natural frequencies are given by (1). For FC-72 and the test cell of $R = 2.5\,\text{cm}$ filled to a depth $h = 3\,\text{cm}$ such that $\tanh(k_{01}h) \cong 1$, the natural frequency of mode (0,1) is $\omega_{01} = [(3.832g/R)(1 + 14.68/Bo)]^{1/2} = 39.08\,\text{rad}\,\text{s}^{-1}$. The capillary contribution to the wave frequency is less than 1 %. In the larger cylinder of $R = 5\,\text{cm}$ and FC-72, $\omega_{01} = 27.419\,\text{rad}\,\text{s}^{-1}$. For the glycerine–water solution, $\omega_{01} = 27.89\,\text{rad}\,\text{s}^{-1}$ and for water $\omega_{01} = 27.99\,\text{rad}\,\text{s}^{-1}$. This assumes that the contact line is free to move, which is not the case for water and glycerine–water solution (see the Appendix). When a 1 %

https://doi.org/10.1017/S0022112008000165 Published online by Cambridge University Press

photo fluid is added to water, the contact line is no longer pinned and surface rigidity is reduced. According to HM, a 1 % photo fluid in water reduces the surface tension to $\sigma \approx 45\,\mathrm{dyn\,cm^{-1}}$.

The natural frequency shift due to linear damping is $\hat{\omega}_{01} = \omega_{01}(1-\delta)$, where $\delta = \kappa/\omega$ is the damping ratio and κ the damping rate. In general, there are two contributions to damping, namely dissipation in the interior δ_i and dissipation in the Stokes layers at the boundaries δ_w. The respective contributions are (Lighthill 1978):

$$\delta \sim (1/R^2)(2\nu/\omega) + (1/R)(\nu/2\omega)^{1/2}. \tag{2a}$$

The ratio of internal to wall damping is, therefore, of the order of $\delta_i/\delta_w \sim 2l_v/R$ where the viscous length scale is the Stokes layer thickness $l_v = (2\nu/\omega)^{1/2}$. For $\omega = \omega_{01}$, the ratio $2l_v/R \cong 2(\nu^2/g^2R^3)^{1/4}$ is of the order of 10^{-2} for FC-72. This small ratio would suggest that viscous dissipation in the Stokes boundary layer dominates over interior dissipation and HM and Henderson & Miles (1994) assumed this to be the case for water in a container of similar size. However, Martel, Nicolas & Vega (1998) and Miles & Henderson (1998) showed theoretically that interior damping might be significant even when $l_v/R \ll 1$, especially when the contact line is pinned, as is the case for water. Miles & Henderson (1998) indicate that discrepancies remain between calculated and experimental damping rates so that it is advisable to measure the damping rate. In the case of glycerine–water, $2l_v/R$ is an order of magnitude larger and internal dissipation is expected to be of importance. We assume $\delta = \delta_\omega$ so that when substituting $\omega = (3.832g/R)^{1/2}$ in (2*a*), we can write the damping ratio in the form:

$$\delta = C(\nu^2/gR^3)^{1/4}, \tag{2b}$$

and determine the constant C from experiments.

In the theory of HM, the wave amplitude as a function of time (at a given spatial position) depends on three control parameters which are the forcing parameter ε, the frequency offset or detuning parameter β and the damping ratio δ. For the axisymmetric mode (0,1)

$$\varepsilon = Ak_{01}\tanh(k_{01}h), \tag{3}$$

$$\beta = \frac{\omega^2 - \hat{\omega}_{01}^2}{2\varepsilon\hat{\omega}_{01}^2}. \tag{4}$$

Steady-state waves exist in the range $-\gamma < \beta < \gamma$, with γ given by:

$$\gamma = [1 - (\delta/\varepsilon)^2]^{1/2}. \tag{5}$$

The stability boundaries are $\beta = \pm\gamma$, with corresponding threshold forcing amplitude:

$$\frac{A}{R} = \frac{1}{3.832\tanh(3.832h/R)}\left[\delta^2 + \frac{\left(\omega^2 - \hat{\omega}_{01}^2\right)^2}{\left(2\hat{\omega}_{01}^2\right)^2}\right]^{1/2}. \tag{6}$$

4. Domain of stationary wave motions and breaking conditions

All the results shown in this section have been obtained in the cylindrical container of $R = 2.5\,\mathrm{cm}$ filled with FC-72 liquid to a depth $h = 3\,\mathrm{cm}$.

4.1. *Damping rate*

For the determination of the instability threshold, it is important to know the damping ratio δ to good accuracy. This ratio can be determined from decay experiments. When

https://doi.org/10.1017/S0022112008000165 Published online by Cambridge University Press

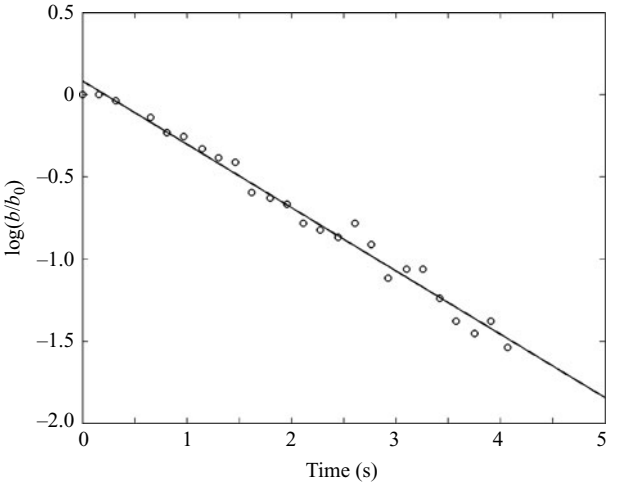


FIGURE 1. Typical decay of the wave amplitude showing the logarithm of b/b_0 as a function of time for $\omega = 38.18\,\mathrm{rad\,s^{-1}}$. The experimental points correspond to the wave amplitude at each period and b_0 is the wave amplitude at the stop of the container forcing. The straight line is a least-squares fit and has a slope of $0.39\,\mathrm{s^{-1}}$.

the wave amplitude was established, the forcing was stopped and the wave motion decayed freely in time. For small damping rate, the decay is exponential and is of the form $b = b_0 \exp(-\delta\omega t)$, where b_0 is the wave amplitude when the forcing is stopped. From images of the wave motion taken at 60 f.p.s., corresponding to a sampling frequency of about ten times the wave frequency, the wave motion was reconstructed by interpolation, giving the successive wave amplitudes to an accuracy of about 3 %. Figure 1 shows the logarithm of wave amplitude as a function of time for the axisymmetric wave mode (0,1) at $\omega = 38.18\,\mathrm{rad\,s^{-1}}$. The decay rate is $\kappa = 0.39\,\mathrm{s^{-1}}$ giving a damping ratio $\delta = \kappa/\omega \cong 0.0102$. From a total of seven decay experiments conducted at frequencies ω near the natural axisymmetric mode frequency ω_{01}, the damping ratio was determined to be $\delta = 0.010 \pm 0.0007$. This value of 0.010 was used for calculating the instability threshold from (6). Using the relation $\hat{\omega}_{01} = \omega_{01}(1 - \delta)$, the natural frequency of the axisymmetric mode after viscosity correction is $\hat{\omega}_{01} = 38.69\,\mathrm{rad\,s^{-1}}$. From here on we drop the circumflex and use for the viscous shifted natural frequency of mode (0,1) the notation $\omega_0 \equiv \hat{\omega}_{01}$.

If it is assumed that damping occurs in the Stokes boundary layers, we find from (2*b*) a value of $\delta = 0.010$ when $C = 1.75$. With this value of C, the damping rate in the HM experiments is $\delta_{HM} = 0.0199$ when using $\nu = 0.01\,\mathrm{cm^2\,s^{-1}}$. This is close to their measured value of $\delta_{HM} = 0.0188$. This agreement does not, however, prove that damping in the interior is insignificant.

4.2. *Parametric instability and wave-breaking thresholds*

Figure 2 shows the dimensionless forcing amplitude instability and wave-breaking thresholds, respectively, A_c/R and A_b/R as a function of ω/ω_0, where subscripts c and b stand for parametric instability onset forcing amplitude and breaking forcing amplitude threshold, respectively, and $\omega_0 \equiv \hat{\omega}_{01}$ (see § 4.1). Wave breaking is defined either by a jet forming or by pinching off the wave crest, followed by irregular (chaotic) motion. The solid line corresponds to (6), with $\delta = 0.010$ and the dotted lines to the inviscid stability boundaries. There is good agreement between the

https://doi.org/10.1017/S0022112008000165 Published online by Cambridge University Press

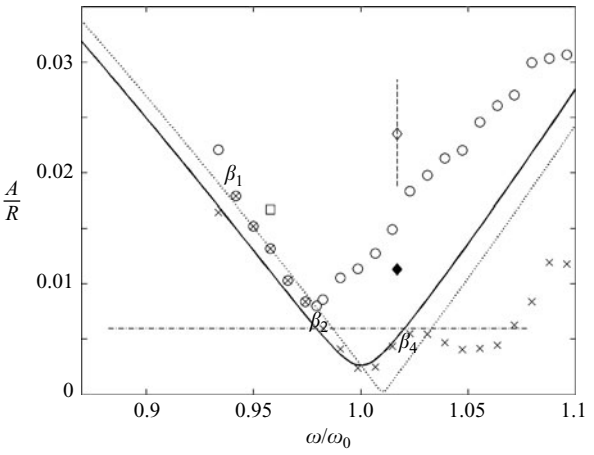


FIGURE 2. Dimensionless forcing amplitude instability and wave-breaking thresholds, respectively, A_c/R (×) and A_b/R (o), as a function of ω/ω_0. The solid curve corresponds to (6) and the dotted curve to the inviscid instability boundary. □, $A/R = 0.0167$, $\omega/\omega_0 = 0.959$; ◇ $A/R = 0.0235$, $\omega/\omega_0 = 1.018$ are the conditions at which the images of jet formation (figure 12) were obtained and ◆, ◇ and the vertical dashed line refer to conditions at which the jet velocity has been measured. The bifurcation points are: $\beta_1 = -0.818$, $\beta_2 = -0.72$, $\beta_4 = 0.90$. The horizontal dashed line corresponds to the conditions of the wave amplitude response curve shown in figure 3.

experimental and calculated instability thresholds in the range $0.94 < \omega/\omega_0 < 1.02$. For $\omega/\omega_0 > 1.02$, the experimental values deviate substantially from the theoretical curve because the wave mode (3,1) is excited. When $\omega/\omega_0 < 0.942$, the wave motion bifurcates to mode (2,1). In general, there is a large difference between the instability threshold forcing amplitude and wave breaking forcing amplitude threshold, except in the range $0.942 \leqslant \omega/\omega_0 < 0.975$ where the two overlap and breaking always occurs just above the instability threshold; in this range, no stable waves exist. This behaviour is indicative of negative nonlinearity of the finite-amplitude resonance frequency response for large fluid depth (Miles & Henderson 1990).

The limits of existence of stable wave motion depend on both the forcing frequency and forcing amplitude related by the frequency-detuning parameter $\beta = (\omega^2 - \omega_0^2)/2\varepsilon\omega_0^2$ (figure 2). The frequency domain of existence of wave breaking increases with forcing amplitude. The minimum wave-breaking threshold is at forcing amplitude $A/R = 0.0079$, $\varepsilon = 0.0303$, giving $\beta = -\gamma = -0.944$ using (5). The corresponding dimensionless frequency is (4)

$$\frac{\omega}{\omega_0} = \left[-2\varepsilon(1 - (\delta/\varepsilon)^2)^{1/2} + 1\right]^{1/2}, \tag{7}$$

and has a value $\omega/\omega_0 = 0.971$. This is close to the experimental value $\omega/\omega_0 = 0.978$, corresponding to $\beta = -0.72$. This wave-breaking bifurcation point is denoted as β_2. At the dimensionless frequency $\omega/\omega_0 = 0.941$, corresponding to $\beta_1 = -0.818$, the wave motion bifurcates to mode (2,1), and $\beta_4 = 0.90$, $\omega/\omega_0 = 1.02$, is the point where bifurcation to mode (3,1) takes place. The bifurcation point β_3 (see figure 9) has not been identified here; it is close to β_2.

https://doi.org/10.1017/S0022112008000165 Published online by Cambridge University Press

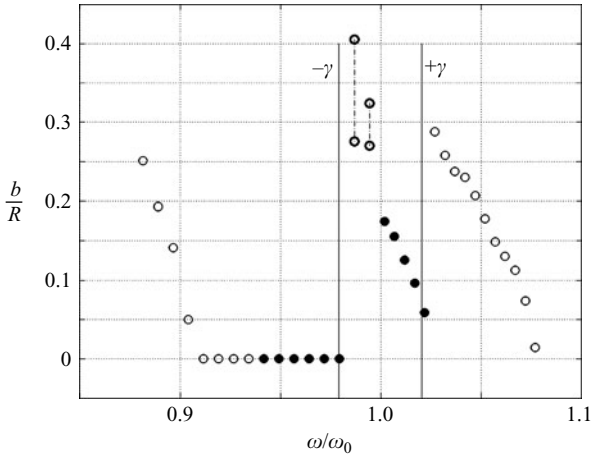


FIGURE 3. Wave-amplitude response for forcing amplitude, $A/R = 0.006$, indicated by the horizontal dashed line in figure 2. ●, steady-state axisymmetric waves; ⚬, the range of the wave-amplitude modulation. The dash-dotted vertical lines connecting the same symbols give the magnitude of the amplitude modulations and the thin solid vertical lines indicate the limits $-\gamma < \beta < \gamma$, equation (5) with $\varepsilon = 0.023$. ○, steady-state asymmetric wave motions of modes (2,1) when $\omega/\omega_0 < 0.942$ and (3,1) above; $+\gamma = 0.90$.

4.3. *Wave-amplitude response*

Figure 3 shows the wave-amplitude response b/R as a function of dimensionless frequency ω/ω_0 for forcing amplitude $A/R = 0.006$ (horizontal dashed line in figure 2). All experimental points correspond to stable wave motions obtained when starting from rest. As will be shown in § 5, the instability is subcritical for $\omega/\omega_0 < 1$ and supercritical for $\omega/\omega_0 \geqslant 1$. The solid bold symbols indicate the existence of steady-state axisymmetric waves and the open symbols refer to mode (3,1) when $\omega/\omega_0 > 1.02$ and to mode (2,1) when $\omega/\omega_0 < 0.942$. Stable axisymmetric wave motions are observed for $-\gamma < \beta < \gamma$, where $\pm\gamma = \pm 0.90$, $\varepsilon = 0.023$ ($A/R = 0.006$), but the wave motion is steady state in a subrange only. Near $-\gamma$, there is an amplitude modulation of the axisymmetric mode (bold open symbols). There is no wave breaking at this forcing amplitude (figure 2).

In figure 4, the amplitude response curves are shown for forcing amplitudes $A/R = 0.006$ to 0.025. As expected from the phase diagram (figure 2), stable axisymmetric wave motion only exists for $A/R < 0.015$, with the frequency range increasing with decreasing forcing amplitude. When $A/R \geqslant 0.015$, only stable asymmetric wave modes exist. Stable axisymmetric waves are bounded by $\beta_2 = -0.72$ ($A/R \cong 0.0079$) with corresponding dimensionless frequency $\omega/\omega_0 = 0.978$ and by $\beta_4 = 0.90$, corresponding to $\omega/\omega_0 = 1.02$. The amplitude modulations of the axisymmetric wave motions are largest at $A/R \approx 0.008$. The maximum frequency range of axisymmetric wave breaking is $0.942 < \omega/\omega_0 < 1.02$. This range decreases when the forcing amplitude is $A/R < 0.015$ and is zero when $A/R \leqslant 0.008$. When, for a given forcing amplitude, say $A/R = 0.020$, the forcing frequency is increased by small increments, starting (figure 4) at $\omega/\omega_0 \approx 0.901$, steady-state asymmetric wave motion of mode (2,1) is observed with the wave amplitude decreasing with increasing forcing frequency until breaking of this wave mode occurs at $\omega/\omega_0 \approx 0.93\,1$. When the forcing frequency is further increased, breaking continues but switches to the axisymmetric mode until the breaking threshold boundary of the asymmetric mode (3,1) is crossed

https://doi.org/10.1017/S0022112008000165 Published online by Cambridge University Press

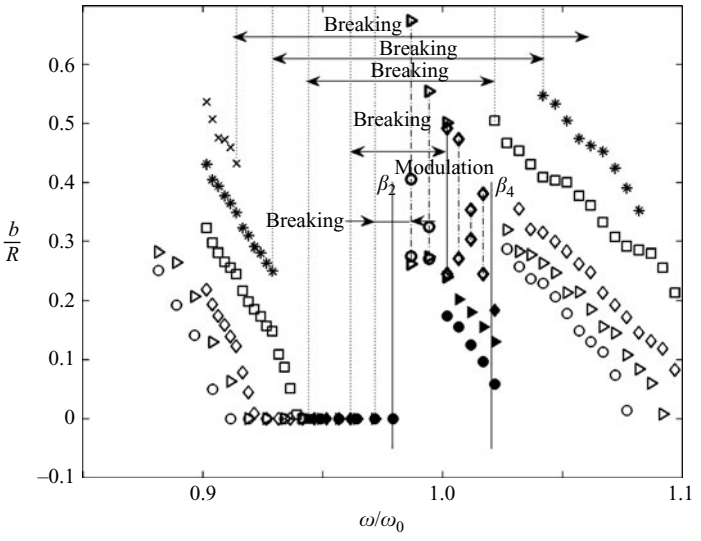


FIGURE 4. Wave-amplitude response curves for forcing amplitudes ranging from $A/R = 0.006$ to 0.025. As in figure 3, the closed symbols indicate steady-state axisymmetric waves: ●, 0.006; ▶, 0.008; ◆, 0.01 and open, bold symbols indicate the range of the wave-amplitude modulation of axisymmetric waves: ⚬, 0.006; ▷, 0.008; ◇, 0.01. The open, light symbols represent steady-state asymmetric wave modes (2,1) and (3,1): ○, $A/R = 0.006$; ▷, 0.008; ◇, 0.01; □, 0.015; ⋆, 0.020 ×, 0.025. The vertical thin dotted lines indicate the wave-breaking limits and the vertical thin solid lines, β_2 and β_4, indicate the limits of stable axisymmetric wave motion.

at $\omega/\omega_0 \cong 1.036$. The behaviour is similar for $A/R = 0.025$, but with an increased frequency range of breaking. For $A/R = 0.015$, the wave amplitude first decreases to zero with increasing forcing frequency and when the breaking threshold is crossed at $\omega/\omega_0 \cong 0.942$, breaking of the axisymmetric wave occurs up to $\omega/\omega_0 \cong 1.020$ where the steady-state wave motion of the asymmetric wave mode (3,1) is reached. For $A/R = 0.01$ and 0.008, the behaviour is similar but with a larger frequency range of zero wave amplitude and narrower range of wave breaking.

4.4. *Amplitude modulations*

The amplitude modulations of the axisymmetric wave mode mentioned above is a slow time scale modulation for forcing amplitudes $A/R = 0.006$ and $A/R = 0.010$ and a period tripling event occurs at forcing amplitude $A/R = 0.008$. This is shown in figure 5 where the wave amplitudes are plotted as a function of dimensionless time t/T, where $T = 2\pi/\omega$. The amplitude modulations in figures 5(*a*) and 5(*c*) are periodic with the period reducing with increasing forcing amplitude. This suggests a slow time scale of the form $\tau = K\varepsilon\pi t/T$, similar to Miles' (1984) slow time scale. For $A/R = 0.006$, $\tau \approx 0.1t/T$ and for $A/R = 0.01$, $\tau \approx 0.18t/T$, giving $K \approx 1.5$. The modulation in wave amplitude in dimensionless time t/T is, therefore, respectively 0.1 and 0.18 of the change in dimensionless slow time τ. This is in good agreement with observations where the half-periods in growth in wave amplitudes are $10t/T$ and $7t/T$. Images of the corresponding wave shapes are shown in figure 6. As expected, the wave crest is more pointed for $A/R = 0.01$ as is seen in figure 6(*b*) where images are shown for $t/T = 1$ and 15; 4 and 18; 8 and 22. For $A/R = 0.006$ (figure 6*a*) the wave crest is almost flat with small-amplitude modulations at the forcing frequency

https://doi.org/10.1017/S0022112008000165 Published online by Cambridge University Press

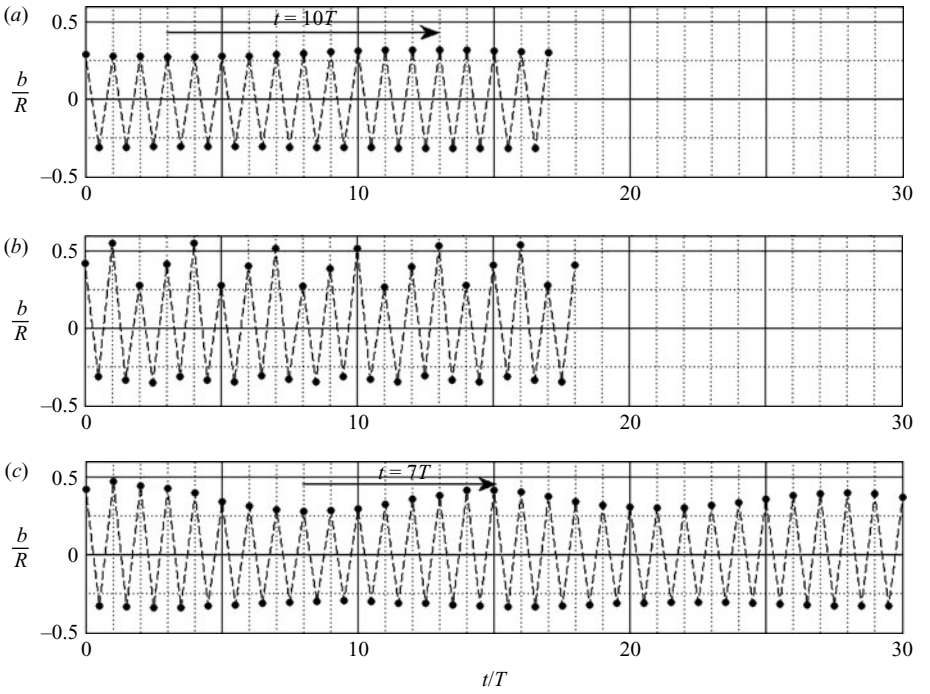


FIGURE 5. Amplitude modulations for different A/R. (*a*) $A/R = 0.006$, $\omega/\omega_0 = 0.994$; (*b*) $A/R = 0.008$, $\omega/\omega_0 = 0.994$; (*c*) $A/R = 0.01$, $\omega/\omega_0 = 1.007$; T is the wave period. The points are the measured wave amplitudes, and the dashed lines join negative and positive amplitudes.

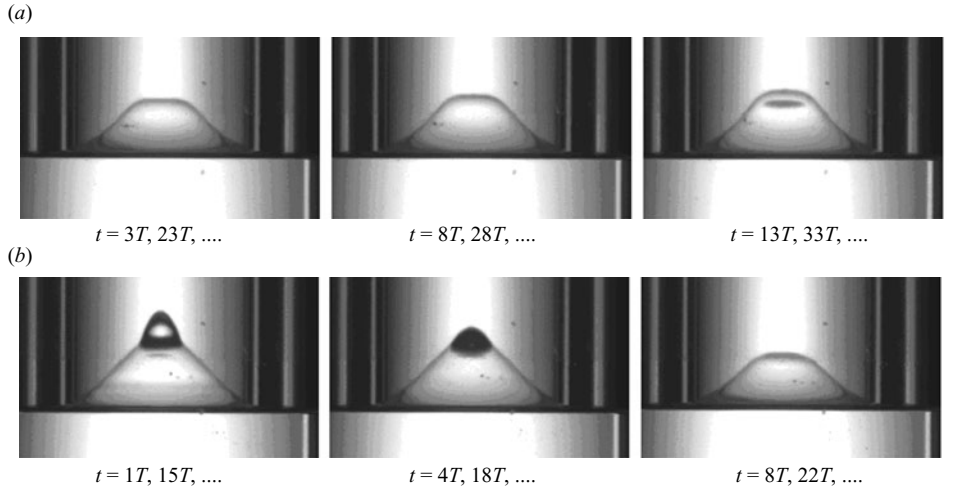


FIGURE 6. Images showing the wave-amplitude modulations for (*a*) $A/R = 0.006$, $\omega/\omega_0 = 0.994$; (*b*) $A/R = 0.01$, $\omega/\omega_0 = 1.007$

.

for which the images are shown. For slightly lower forcing frequency, the amplitude modulations are larger, as seen in figure 4, but remain similar to figure 6(*a*).

The period tripling event at $A/R = 0.008$ is demonstrated in figure 7. The event is visualized in the images shown in figure 7(*a*). It is seen that the wave crest steepens, is flat-topped in the next period and then takes an intermediate amplitude before

https://doi.org/10.1017/S0022112008000165 Published online by Cambridge University Press

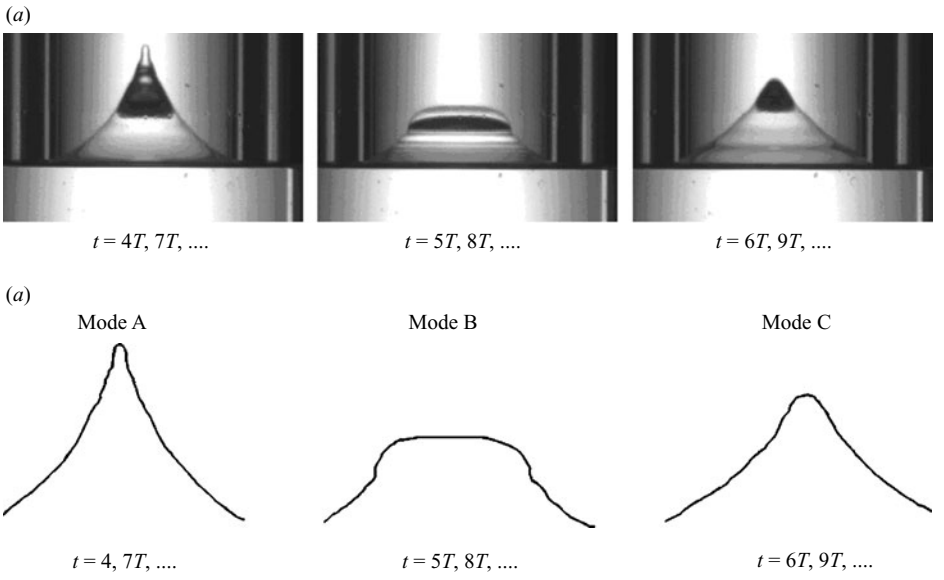


FIGURE 7. Images showing the wave-amplitude modulations for the conditions shown in figure 5(*b*). (*a*) Period tripling scenario; (*b*) contours of the wave shapes traced from the images (with the scale slightly enlarged).

the cycle begins again. The wave shape contours are traced in figure 7(*b*) (somewhat enlarged with respect to the images). This period tripling is similar to the period tripling event observed by Jiang *et al.* (1998) for two-dimensional waves, except that in the present experiments there is no wave breaking or spilling associated. It is most likely that capillary forces that are stronger in the axisymmetric case prevent the wave from breaking. The downward acceleration by the capillary forces is, however, only a fraction of the acceleration due to gravity (about $0.1g$). The wave amplitude b_c at which the downward acceleration is equal to gravity is $b_c = g/\omega_0^2 \cong 0.26R$ and it can be seen in figure 4 that the wave crest can reach twice this value. Therefore, it is expected that a lump of fluid falls nearly freely under gravity and impinges on the upward-moving wave crest during the next period causing the wave top to flatten and dissipate wave energy.

Figure 8 shows the amplitude modulation for $A/R = 0.008$ and $\omega/\omega_0 = 0.986$ just before breaking or jet formation. A sequence of images (figure 8*b*) shows period tripling with a large variation in amplitude. However, period tripling events observed at this frequency are not continuous (figure 8*a*). In the time series $t/T = 0$ to 30, no period tripling occurs in $t/T = 4$ to 6 and 16 to 18, whereas successive period tripling events occur for $t/T = 1$ to 3, 7 to 15 and 19 to 30.

5. Supercritical and subcritical instabilities

In this section, results of the nature of the instability are presented for the low-viscosity liquid FC-72 in the larger container of $R = 5$ cm filled to a depth $h = 6$ cm. The larger container is used here because the resolution is somewhat improved when the container is larger and damping is less. Note that this container has been constructed for the purpose of clarifying the possible effect of surface tension on jet formation presented in § 6.

https://doi.org/10.1017/S0022112008000165 Published online by Cambridge University Press

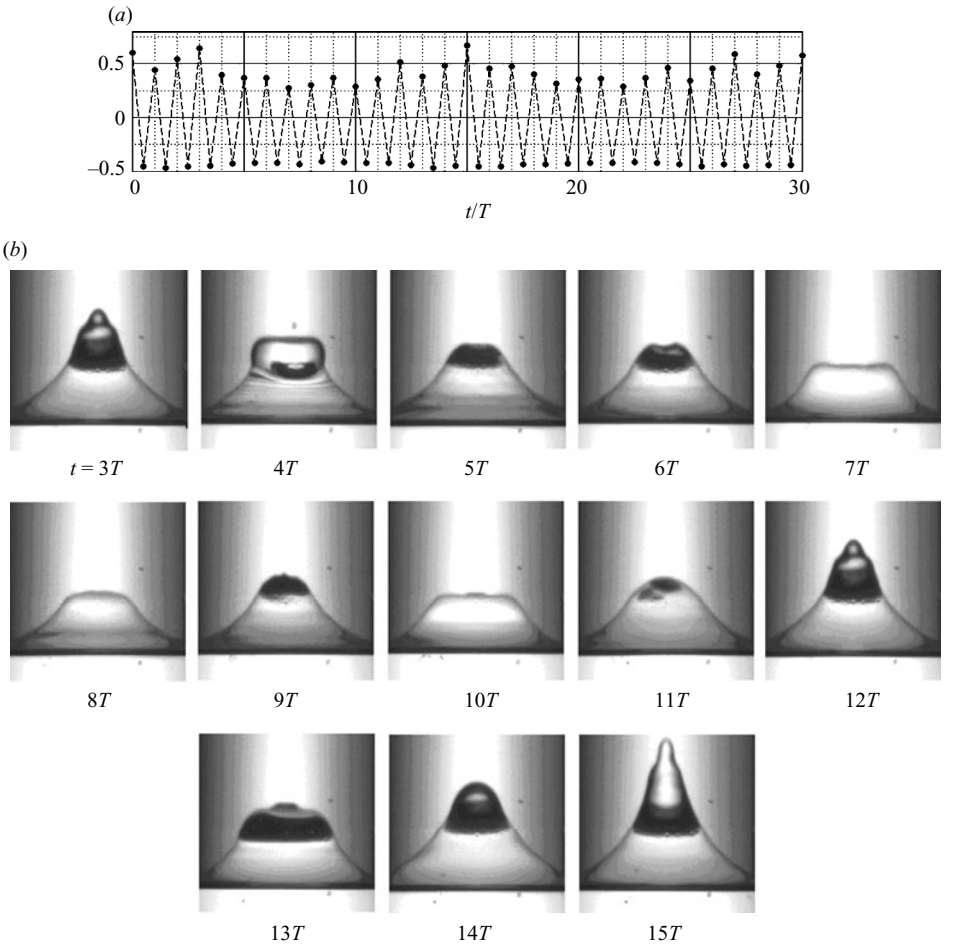


FIGURE 8. Amplitude modulations for $A/R = 0.008$ and $\omega/\omega_0 = 0.986$. (*a*) Wave amplitude as a function of time showing amplitude modulations; (*b*) images showing different stages of the modulations with and without period tripling.

5.1. *Parametric instability threshold*

The forcing amplitude instability threshold as a function of dimensionless wave frequency is shown in figure 9 for FC-72. As in figure 2, the axisymmetric mode (0,1) exists in the range $0.94 < \omega/\omega_0 < 1.020$ and there is good agreement with the theoretical prediction (6) shown by the solid curve in figure 9. It should be noted that as in figure 2, the experimental points are slightly above neutral stability where perceptible but no measurable wave motion exists (wave amplitude of 0.1 to 0.2 mm). This means that, in the frequency range where the instability and breaking thresholds coincide, the wave amplitude at the experimental points indicated, will grow and eventually break. The neutral stability boundary is very close to the experimental points (about 1 % below). The value of the damping ratio used in fitting the theoretical curve is $\delta = 0.0022$. The value obtained from (2*a*) with $C = 1.75$ is 0.0059. We have conducted two decay experiments that give a value $\delta \approx 0.0022$, hence $C \approx 0.6$. This seems to indicate that in the smaller container, internal damping is of importance whereas in the $R = 5$ cm container,

https://doi.org/10.1017/S0022112008000165 Published online by Cambridge University Press

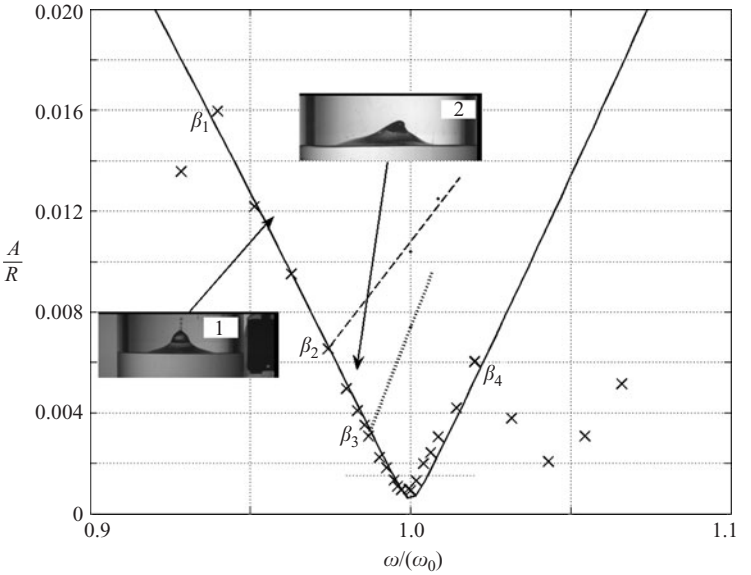


FIGURE 9. Dimensionless forcing amplitude instability thresholds as a function of ω/ω_0 for FC-72 in the $R = 5$ cm container. The solid line corresponds to the theoretical curve (6) with $\delta = 0.0022$. Bifurcation points are: bifurcation to mode (2,1), $\beta_1 = -0.962$, $\omega/\omega_0 = 0.94$; wave-breaking bifurcation, $\beta_2 = -1.015$, $\omega/\omega_0 = 0.974$; unsteady wave motion, $\beta_3 = -0.753$, $\omega/\omega_0 = 0.987$; bifurcation to mode (3,1), $\beta_4 = 0.875$, $\omega/\omega_0 = 1.02$; β is defined by (6). - - -, experimental wave breaking threshold; $\cdots$, onset of unstable wave motion.

internal damping is negligible. The linear damping corrected resonance frequency is $\omega_0 \equiv \hat{\omega}_{01} = \omega_{01}(1-\delta) = 27.419(1-0.0022) = 27.358\ \mathrm{rad\,s^{-1}}$.

At $\omega/\omega_0 = 1.020$, $\beta_4 = 0.875$, the wave motion bifurcates to the wave mode (3,1) of dimensionless wavenumber $k_{31}R = 4.201$ and of linear damping shifted frequency $\omega_{31} = 28.69\ \mathrm{rad\,s^{-1}}$. In figure 9, the natural frequency of this mode is, therefore, at $\omega/\omega_0 = 1.0496$. In the range $0.94 \leqslant \omega/\omega_0 < 0.974$, $\beta_1 \geqslant \beta > \beta_2$, where $\beta_1 = -0.962$ and $\beta_2 = -1.015$, the wave motion is unstable when the parametric instability threshold is crossed with exponential growth in wave amplitude up to breaking (inset image 1) with possible jet formation. In the interval $0.974 \leqslant \omega/\omega_0 \leqslant 0.987$, $\beta_2 \leqslant \beta \leqslant \beta_3$, where $\beta_3 = -0.753$, the wave motion is unstable above the instability threshold but the amplitude remains finite (inset image 2). In the range $0.987 < \omega/\omega_0 \leqslant 1.020$, the instability is subcritical for $\omega/\omega_0 < 1$ and supercritical at $\omega/\omega_0 = 1$ and above (see § 5.2). Because of smaller damping in the $R = 5$ cm container, the values of the bifurcation points differ from the values in the $R = 2.5$ cm container.

5.2. *Instability behaviour*

In figure 10, the dimensionless wave amplitude is plotted as a function of the control parameter

$$\alpha = \frac{A - A_c}{A_c}, \tag{8}$$

for values of $\omega/\omega_0 = 0.9994$, 1.0086 and 0.9926, first by increasing and then decreasing the forcing amplitude by small steps. The value of A_c in (8) is given by the stability threshold shown in figure 9 at the frequency considered. At the natural frequency and above, the instability is clearly supercritical with the wave amplitude, proportional to

https://doi.org/10.1017/S0022112008000165 Published online by Cambridge University Press

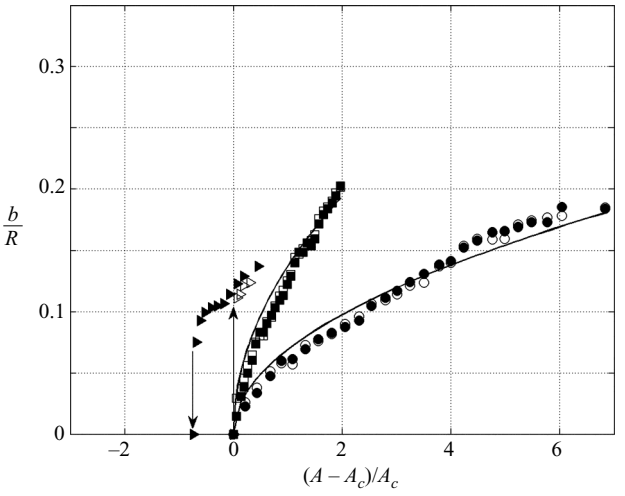


FIGURE 10. Dimensionless wave amplitude as a function of the control parameter α (8), for ○, $\omega/\omega_0 = 0.9994$; □, 1.0086; △, 0.9926. The open symbols indicate increasing forcing amplitude A by small increments ΔA and the solid symbols indicate decreasing forcing amplitude. The time interval between each increment and decrement is about 100 s. The curves fitted through the experimental data at $\omega/\omega_0 = 0.9994$ and 1.0086 are, respectively, $b/R = 0.069\alpha^{12}$ and $b/R = 0.137\alpha^{12}$; $R = 5$ cm.

the fluid velocity, increasing as $\alpha^{1/2}$. The prefactor depends on ω/ω_0. At $\omega/\omega_0 = 0.9994$, $b/R = 0.069\alpha^{12}$ and at $\omega/\omega_0 = 1.0086$, $b/R = 0.137\alpha^{1/2}$. The maximum value of α is limited by the onset of amplitude modulations. Below the natural frequency ($\omega < \omega_0$), the instability is subcritical. When at $\omega/\omega_0 = 0.9994$, the instability threshold A_c is crossed by increasing the forcing amplitude by small increments, the wave amplitude increases suddenly to $b/R \approx 0.11$. Then it continues to increase slowly with increasing forcing amplitude. The maximum value of α is in this case limited by the unsteady wave motion threshold. When the forcing amplitude is then decreased in small steps, the wave amplitude decreases slowly down to $b/R \approx 0.075$ and then drops to zero at $\alpha \cong -0.739$.

The subcritical behaviour for $\omega/\omega_0 < 1$ is demonstrated well by figure 11, where the wave amplitude is plotted as a function of ω/ω_0 for a forcing amplitude $A/R = 0.0015$. A finite-amplitude wave motion is first established by starting at $\omega/\omega_0 = 0.999$. When the forcing frequency is then decreased by small steps, the wave amplitude increases until the instability threshold is crossed, beyond which it continues to increase with decreasing forcing frequency down to $\omega/\omega_0 \cong 0.986$ where it drops to zero suddenly. When ω/ω_0 is then increased, the wave amplitude remains zero until the instability threshold is reached where it increases rapidly. There is a clear hysteresis loop consistent with the subcritical behaviour shown in figure 10 for $\omega/\omega_0 < 1$. On the contrary, when the forcing frequency is increased starting at $\omega/\omega_0 = 1$ the wave amplitude decreases until the instability threshold is crossed and then drops to zero, consistent with the supercritical instability at $\omega/\omega_0 \geqslant 1$. Benielli & Sommeria (1998) determined a similar behaviour of the asymmetric internal wave mode (1,1) for parametrically forced internal waves at a density interface and Dodge (1966) showed the existence of a hysteresis loop for the surface wave mode (1,1). In a narrow rectangular channel, Jiang *et al.* (1996) showed the existence of a hysteresis loop that

https://doi.org/10.1017/S0022112008000165 Published online by Cambridge University Press

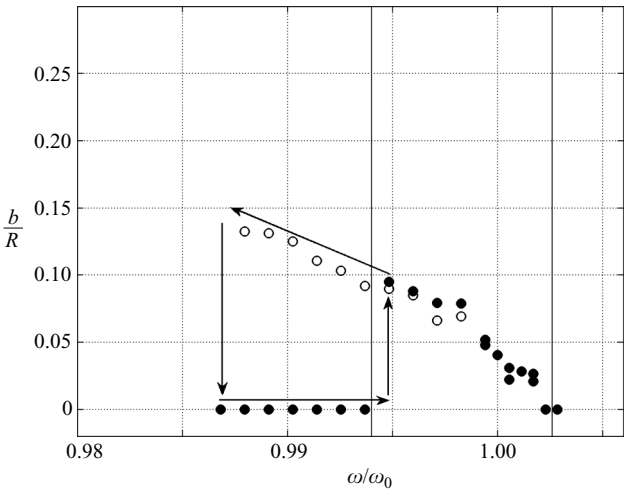


FIGURE 11. Dimensionless wave amplitude versus forcing frequency for $A/R = 0.0015$. ○, decreasing frequency starting at $\omega/\omega_0 = 0.9994$; ●, increasing frequency. The arrows indicate the sense of the hysteresis loop. Vertical solid lines indicate cross-over frequencies of the instability curve (figure 9).

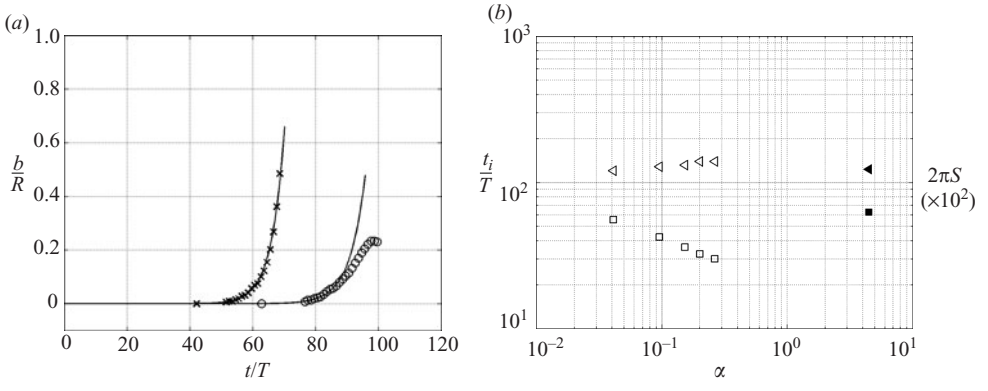


FIGURE 12. (*a*) Wave-amplitude growth versus time. ×, breaking regime, $\omega/\omega_0 = 0.963$, $A/R = 0.0113$, $t_i/T = 42$; ○, steady-state wave regime, $\omega/\omega_0 = 1$, $A/R = 0.005$, $t_i/T \approx 63$. The solid lines represent the exponential fits. (*b*) Time of onset of wave motion t_i (□, ■) and amplification rate s (▷, ▶) versus the control parameter α. The solid symbols are for the steady wave regime; $T = 2\pi/\omega$.

was attributed to contact line effects. Note that just beyond the bifurcation point to mode (3,1), that is at $\omega/\omega_0 = 1.02$, the instability of mode (3,1) is again subcritical.

The temporal growth in wave amplitude above the instability threshold is exponential. From figure 12(*a*), this is clear in the frequency range where the instability and breaking thresholds coincide ($0.94 \leqslant \omega/\omega_0 < 0.974$) and the wave amplitude grows until breaking. In the stable wave regime, the growth is exponential only initially and then changes to a nearly linear growth before reaching the stable wave amplitude. However, in both regimes, when starting from rest at time $t = 0$ in figure 12(*a*), this onset in exponential growth occurs only after a certain time, denoted as t_i. In the typical examples shown in figure 12(*a*), the exponential growth in wave amplitude for $\omega/\omega_0 = 0.963$, $A/R = 0.0113$ starts at $t_i/T \approx 42$ and in the stable wave regime,

https://doi.org/10.1017/S0022112008000165 Published online by Cambridge University Press

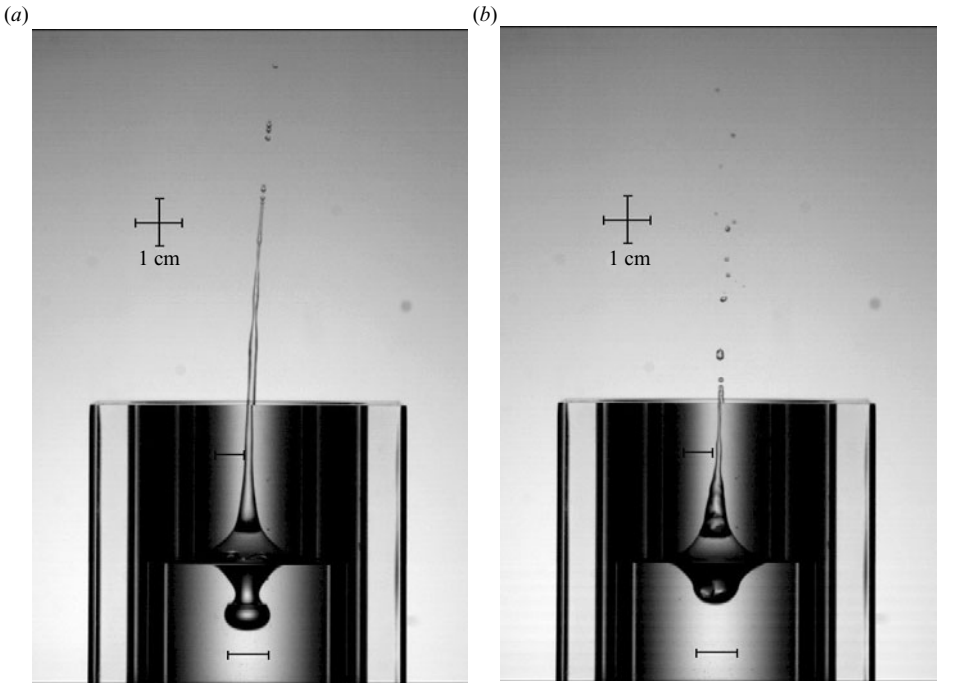


FIGURE 13. A composite of two photographs showing the axisymmetric wave depression (cavity) below and jet formation above for (*a*) $A/R = 0.0167$, $\omega/\omega_0 = 0.959$; (*b*) $A/R = 0.0235$, $\omega/\omega_0 = 1.018$. The horizontal and vertical bars represent 1 cm. Note that the horizontal scale changes somewhat with location because of optical distortions. $R = 2.5$ cm, FC-72 liquid.

$\omega/\omega_0 = 1$, $A/R = 0.005$ at $t_i/T \approx 63$. Before this time t_i there is no discernible motion of the free surface in the centre of the container.

The growth rate can be written as $b/R = (b_i/R)\exp(s\omega(t - t_i))$ where s is the dimensionless amplification rate and b_i the initial wave amplitude at t_i. In the breaking regime at frequency $\omega/\omega_0 = 0.963$, we determined the amplification rate s and the onset time t_i for different values of $\alpha = (A - A_c)/A_c$ (figure 12*b*). t_i decreases with increasing α and the amplification rate slightly increases. In the stable wave regime it takes a longer time (solid square symbol) before the wave amplitude starts to grow. The growth rate (solid triangle) is similar to that in the breaking regime.

6. Jet formation: finite-time singularity

For container forcing amplitudes $A > A_b$, wave breaking occurs. Axisymmetric wave breaking may lead to high-velocity jet formation. The jet is formed by the collapse of the depression or cavity caused by the large-amplitude axisymmetric standing wave, a phenomenon observed by Longuet-Higgins (1983) and analysed by Zeff *et al.* (2000). Images of the wave depression (lower part of image) and of jet formation (upper part of image) are shown in figure 13 for two different forcing conditions; these conditions are indicated in figure 2 by □ and ◇.

The question is whether this jet formation depends on surface tension. Zeff *et al.* developed a similarity theory and a power-law scaling in $(t - t_0)^{\pm 2/3}$ of the free-surface displacement and of the velocity potential (where t_0 is the time at which the singularity occurs) to calculate the form of the free-surface depression near t_0.

https://doi.org/10.1017/S0022112008000165 Published online by Cambridge University Press

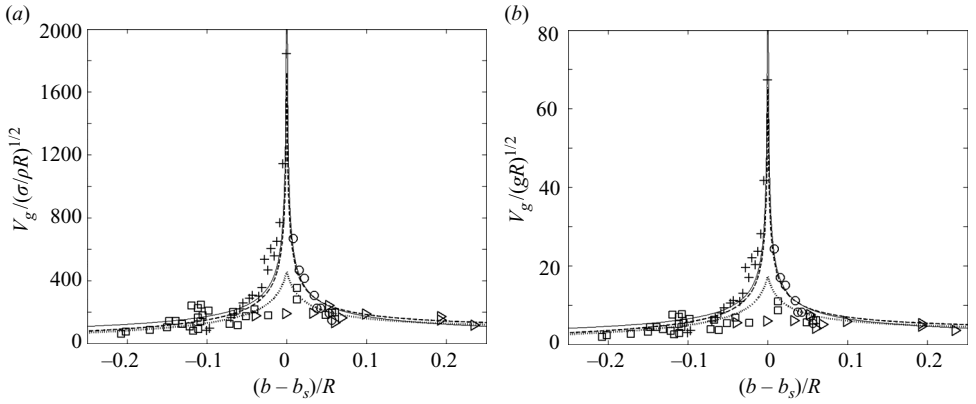


FIGURE 14. Dimensionless jet velocity versus the last smooth standing-wave amplitude ($(b-b_s)/R$) at $\omega/\omega_0 = 1.018$; □, without bubble pinch-off; ▷, with pinch-off. (*a*) Jet velocity made dimensionless by the surface tension velocity scale, $V_g/(\sigma/\rho R)^{1/2}$ and (*b*) jet velocity made dimensionless by the inertial velocity scale (wave fluid velocity), $(gR)^{1/2}$. The solid line in (*a*) is the Weber number correlation (9) and the dotted lines are correlation (10) for $r_s = 3$ mm and dashed lines for $r_s = 2$ mm. The solid, dotted and dashed lines in (*b*) are the Froude number correlations (11) and (12), respectively. $b_s/R \cong 0.88$, $b_s\omega = 84.87\,\mathrm{cm\,s^{-1}}$, $(\sigma/\rho R)^{1/2} = 1.61\,\mathrm{cm\,s^{-1}}$. +, O, Zeff *et al.* $(\sigma/\rho R)^{1/2} = 2.85\,\mathrm{cm\,s^{-1}}$, $b_s/R = 0.968$.

This scaling introduces a Weber number and the experiments of Zeff *et al.* seem to indicate that the maximum jet velocity, V_g, scales with the Weber number in the form $We = \rho V_g^2(b-b_s)/\sigma$, where b_s is the maximum stable wave amplitude above which bubble pinch-off (figure 13*a*) takes place at the wave depression. The value of the critical Weber number is not given, but the experimental results of Zeff *et al.* suggest a value of $We_c \approx 3000$. The container radius should enter into the scaling because the critical wave amplitude b_s must depend on R. Viscous cutoff prevents V_g from becoming infinite as $b \to b_s$. A non-smooth surface has a similar cutoff effect to viscosity. This is the case with water where perturbations in the form of parasitic capillary waves appear. Zeff *et al.* used a container of radius $R = 6.35$ cm and a glycerine–water solution of $\nu = 1.94\,\mathrm{cm^2\,s^{-1}}$ to keep the surface smooth at large wave amplitudes. With the low-viscosity fluid FC-72, parasitic capillary waves are reduced because of the low kinematic surface tension. Generally, a stationary wave motion was first established at $A/R = 0.012$ and $\omega/\omega_0 \cong 1.018$ (◆ in figure 2) and then the forcing amplitude was increased above the wave-breaking threshold amplitude A_b. Experiments done at $\omega/\omega_0 \cong 0.959$ (□ in figure 2), where no stable axisymmetric wave motion exists, lead practically to the same jet formation.

In order to be able to compare results obtained with different container sizes and different fluid properties, it is necessary to develop a dimensionless expression for the jet velocity. If we use the Weber number criterion as suggested by Zeff *at al.*, the following dimensionless scaling law can be established:

$$\frac{V_g}{(\sigma/\rho R)^{1/2}} = \left[We_c \frac{R}{b|(1-b_s/b)|}\right]^{1/2}. \tag{9}$$

In figure 14(*a*), we plot this dimensionless jet velocity $V_g/(\sigma/\rho R)^{1/2}$ as a function of b/R, where b is the last 'stable' wave amplitude before cavity formation and sudden jet emergence. The solid lines in figure 14(*a*) are for $We_c = 3000$ in (9) that best fits

https://doi.org/10.1017/S0022112008000165 Published online by Cambridge University Press

the data of Zeff *et al.* The corresponding critical wave amplitude is $b_s/R = 0.968$, whereas the present data are best fitted by $b_s/R = 0.88$. Although the dispersion in the measured velocities is large, the relatively good collapse of the present results with the results of Zeff *et al.*, obtained for a kinematic surface tension ten times larger ($\sigma/\rho \approx 65\ \mathrm{cm^3\,s^{-2}}$), would indicate that the jet velocity scales with surface tension. The agreement is less good when the singularity is approached ($b \to b_s$), which would suggest that in a larger container the singularity is more pronounced. One possible argument is that the wave depression, that is the radius of the cavity r_s, just before jet emergence, is finite and is, to first approximation, independent of container radius. Thus when r_s/R is small, the jet velocity is larger. We can add this finite-size effect in (9) in the form:

$$\frac{V_g}{(\sigma/\rho R)^{1/2}} = \left[We_c \frac{R}{b|(1 - b_s/b)| + r_s^2/R}\right]^{1/2}. \tag{10}$$

The experimental data obtained in a container of size $R = 2.5$ cm are best fitted by a cavity radius (quasi-singularity) at jet emergence of $r_s \approx 3$ mm. The jet velocities according to (10) with $r_s \approx 3$ mm are shown by the dotted lines in figure 14. This has the correct behaviour, but in order to reach the largest jet velocity measured by Zeff *et al.* the cavity radius has to be reduced to about $r_s \approx 2$ mm (dashed lines in figure 14).

The distinction between the right-hand and left-hand branches in figure 14 is that there is bubble detachment when $(b - b_s)/R > 0$ (figure 13*a*). The data by Zeff *et al.* show this distinction clearly, whereas in the present data the dispersion is larger. We kept all data to show that the jet velocities are not always identical for the same experimental conditions; small perturbations can become significant.

In figure 14(*a*), the jet velocity is two to three orders of magnitude larger than the surface tension velocity scale $(\sigma/\rho R)^{1/2}$. Even if R is replaced by the radius r_s at which surface tension forces act, the jet velocity is still one to two orders of magnitude larger than the surface-tension generated velocity. This suggests that the driving force is inertia. The jet velocity can in this case be scaled by a modified Froude number of the form $V_g/(gR)^{1/2}/((b - b_s)/R) = Fr$. In figure 14(*b*), the jet velocity is scaled with $(gR)^{1/2}$ and plotted as a function of $(b - b_s)/R$ as in figure 14(*a*). The solid line in figure 14(*b*) is the correlation

$$\frac{V_g}{(gR)^{1/2}} = \left[Fr_c \frac{R}{b|(1 - b_s/b)|}\right]^{1/2}, \tag{11}$$

with the characteristic Froude number $Fr_c = 4.3$. The dotted and dashed lines are the finite-size cavity correlation with, respectively, $r_s = 3$ mm and 2 mm in the correlation:

$$\frac{V_g}{(gR)^{1/2}} = \left[Fr_c \frac{R}{b|(1 - b_s/b)| + r_s^2/R}\right]^{1/2}. \tag{12}$$

The scaling with $(gR)^{1/2}$ collapses the data nearly as well as the surface tension scaling and the numerical values of the dimensionless jet velocity are physically more plausible. The reason for the collapse of the data in both scalings is that by coincidence the ratio of $\sqrt{\sigma/\rho R}$ and the square root of the radii in the present and the Zeff *et al.* experiments differ only by about 20 %. Therefore, the good collapse by the Weber number scaling is not conclusive.

In the falling, partially filled, coffee cup experiment of Milgram (1969), surface tension is required to curve the free surface during the free fall, but the jet is formed

https://doi.org/10.1017/S0022112008000165 Published online by Cambridge University Press

by the gravity wave generated when the cup impacts on the ground which propagates radially inward and forms a central cavity; the inertial collapse of this cavity generates an intense jet. A similar jet by inertial cavity collapse is observed in dam break experiments in a cylindrical container where a gravity wave propagates toward the centre after sudden withdrawal of the barrier (Hopfinger & Baumbach 2007). When a wave impacts on a vertical wall, a two-dimensional jet is formed (Peregrine *et al.* 2004). In these situations, as the air cavity forms there is a phenomenon called flip-through.

In the present standing-wave experiments, the cavity is formed by the downward acceleration of the large-amplitude axisymmetric wave crest column. When the wave amplitude is large, a fluid column (part of the wave crest) falls under gravity and surface tension forces and impinges at the wave trough, forming a cavity. In order to clarify the possible influences of container size and of surface tension on this mechanism, we performed further experiments in the container of $R = 5\,\mathrm{cm}$ with FC-72, glycerine–water solution and some with distilled water (in the small container, experiments with glycerine–water were not conclusive because of too much damping). The forcing amplitude stability thresholds for glycerine–water and water as well as water with photo fluid are given in the Appendix. Figure 15 shows, for the three liquids, typical shapes of the last stable wave crests as well as the cavities, which form half a period later at the wave trough. On (inertial) collapse of these cavities the intense jet emerges. Clearly, surface tension and viscosity (if the Ohnesorge number is of order 1 as it is for glycerine–water) affect the shape of the wave crests and, consequently the cavity size by inhibiting parasitic capillary waves and by preventing Taylor instability from developing. Taylor showed that a free surface, hence a wave crest, is unstable when the downward acceleration exceeds gravity g (Taylor 1950). Milgram (1969) extended the theory of Taylor by including the effect of surface tension and showed that the free surface is unstable when the downward acceleration exceeds gravity plus the acceleration due to surface tension. For the axisymmetric wave, downward acceleration due to surface tension is in the linear limit equal to $(\sigma/\rho)k_{01}^2$. As the wave amplitude grows, the curvature of the wave crest increases, hence increasing the surface tension contribution. Rayleigh instability is not possible because the shortest wavelength that could be amplified exceeds $2\pi r_1$.

It can be seen from figure 15(a) that the large viscosity of glycerine–water solution inhibits parasitic capillary waves and Taylor instability. The fluid column is smooth and has a smaller diameter. The cavity that is formed (lower part of image) when the wave column is accelerated downward, and impinges on the wave trough, is deeper and of smaller size than in water and FC-72. Its aspect ratio, that is cavity depth to cavity radius, is $\ell/r_{ca} \geqslant 1$. The cavity size, of radius r_{ca}, shown in the images corresponds to the instant when the cavity just begins to contract. When the kinematic surface tension is small as in FC-72 (figure 15d, e) a cylindrical precursor fluid column is projected upward (Taylor instability) that is then partially or completely taken over by the following wave crest; drop pinch-off may occur in some cases (figure 15d) or the wave crest may be flat-toped (figure 15e). Parasitic capillary waves are insignificant. With water (figure 15b, c) this upward projection of a cylindrical fluid column also happens, but is less pronounced because of higher surface tension. Parasitic capillary waves are clearly present (figure 15b taken at $0.186T$ before figure 15c) but because of the high surface tension, the wave crest remains axisymmetric. The wave shape shown in image 15(f) is for FC-72 and container radius $R = 2.5\,\mathrm{cm}$ resulting in a lower Bond number and, hence, a smoother wave crest. The characteristic values of the wave crest and of the cavity are summarized in table 1.

https://doi.org/10.1017/S0022112008000165 Published online by Cambridge University Press

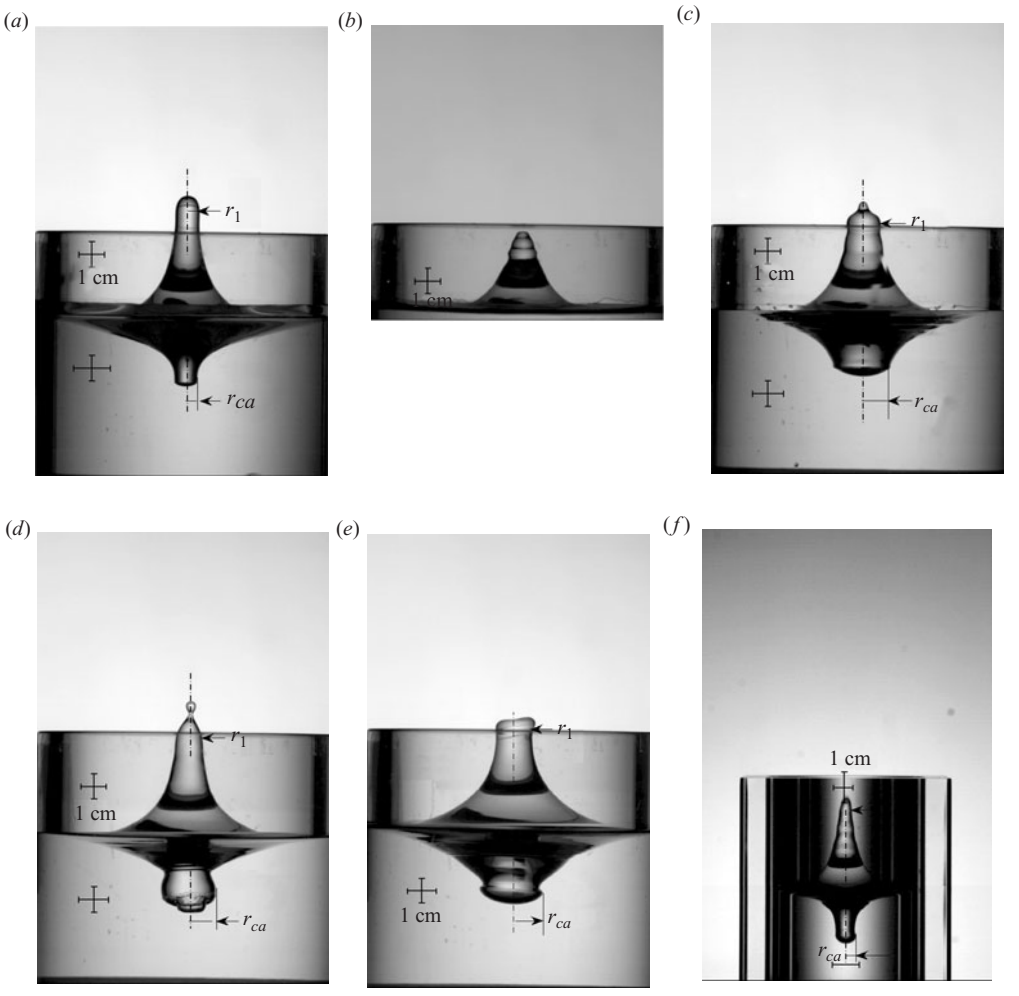


FIGURE 15. Composite images (*a*, *c*–*e*) obtained in container $R = 5$ cm and image (*f*) obtained in container $R = 2.5$ cm, showing the last stable wave amplitude and the following (half a period later) wave depression (cavity) below, for glycerine–water (*a*), water (*c*) and FC-72 (*d*, *e*). (*b*) The wave crest for water, with parasitic capillary waves, taken at 0.186 wave period before the maximum wave amplitude is reached, shown in (*c*); (*a*) $\omega_f/2\pi = 8.85$ Hz, $A/R = 0.0368$; (*c*) $\omega_f/2\pi = 8.86$ Hz, $A/R = 0.0154$; (*d*) $\omega_f/2\pi = 8.77$ Hz, $A/R = 0.0179$;(*e*) $\omega_f/2\pi = 8.35$ Hz, $A/R = 0.0143$; (*f*) $R = 2.5$ cm, FC-72, $\omega_f/2\pi = 11.65$ Hz, $A/R = 0.0175$.

In figure 16, dimensionless jet velocities ($V_g/\sqrt{gR}$) are shown as a function of $(b-b_s)/R$ for the three liquids in the container of $R = 5$ cm. The first observation is that the jet velocity scales with the Froude number because for FC-72 the dimensionless velocity is nearly the same in containers of $R = 2.5$ cm (figure 14*b*) and of $R = 5$ cm. Furthermore, in water of about ten times larger kinematic surface tension, the jet velocity is only about 40 % larger (and not by a factor of 3 as surface tension scaling would suggest) than in FC-72. The reason is that the contribution of surface tension to the downward acceleration is larger in water than in FC-72 (table 1). With glycerine–water, a much larger jet velocity can be achieved. This is because the last stable wave crest is of larger amplitude and has a smaller radius. In addition, it remains smooth (figure 15*a*) because the large viscosity prevents parasitic capillary waves and

https://doi.org/10.1017/S0022112008000165 Published online by Cambridge University Press

	σ/ρ (cm^3 s^{-2})	ν (cm^2 s^{-1})	R (cm)	T (s)	r_1 (mm)	r_{ca} (mm)	ℓ/r_{ca}	$\frac{\sigma}{\rho g r_1^2}$	t_{cr} (s)	a_{cr}/g
			2.5	0.17	2.7	4	1.05	0.09	0.056	1.16
FC-72	6.5	0.0040	5	0.23	5.5	9.5	–	0.02	–	–
			5	0.24	7	11.1	0.59	0.01	0.064	1.09
Glycerine–water	65	2.5	5	0.23	4.5	3.2	2.14	0.3	0.079	1.16
Water	71	0.01	5	0.23	6	9.5	0.32	0.2	0.059	1.3

TABLE 1. Summary of the fluid properties, wave crest radius, r_1, cavity radius, r_{ca}, and of cavity aspect ratios ℓ/r_{ca}. a_{cr} is the measured downward acceleration of the wave crest before cavity formation and t_{cr} is the time it takes for the wave crest to move downward by a distance R. the wave period is $T = 2\pi/\omega$.

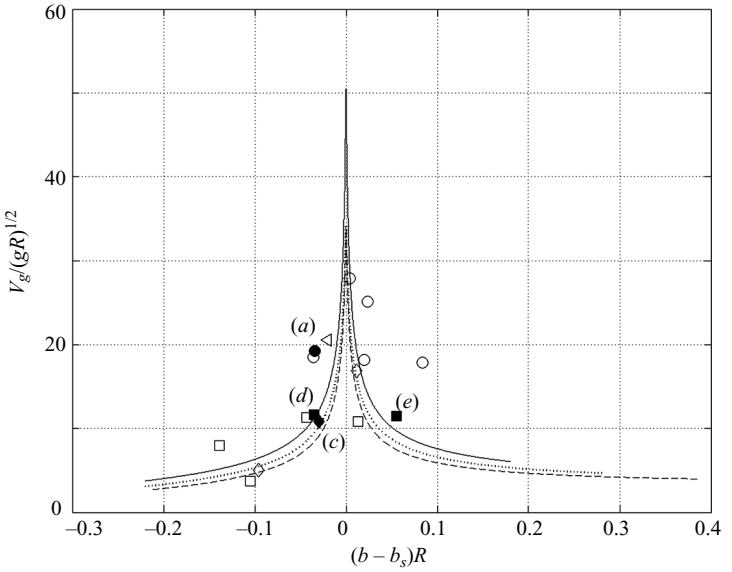


FIGURE 16. Dimensionless jet velocity versus $(b - b_s)$/R, where b is the last stable wave amplitude before jet formation. ○, glycerine–water; □, FC-72; ◇, distilled water. Filled symbols with letters next it, are the velocities corresponding to the images shown in figure 15. The wave amplitude b_s above which bubble pinch-off occurs (figure 13a) is $b_s/R \approx 0.815$, 0.92 and 1.07 for, respectively, FC-72, water and glycerine water. The data are best fitted by (12) with $r_s = 3$, 3, 2 mm, respectively, for FCg-72 (- - -), water (. . .), and glycerine–water (———). With water–photo fluid solution, $b_s/R = 1$, point ◁, the experiment has been done for forcing amplitude $A/R = 0.013$ and forcing frequency $\omega_f/2\pi = 8.4$ Hz.

Taylor instability. The cavity that forms is consequently smaller and deeper (larger aspect ratio ℓ/r_{ca}). It is not surface tension that is responsible for the larger cavity aspect ratio, hence larger jet velocity, because the contribution of surface tension to the downward acceleration of the wave crest, a_{cr}, is less than in water (table 1). Furthermore, the upward acceleration by surface tension in the cavity is negligible compared with the wave acceleration and especially compared with the acceleration required to produce the high-velocity jet.

https://doi.org/10.1017/S0022112008000165 Published online by Cambridge University Press

In figure 16, it can be seen that the jet velocities are reasonably well fitted by (12) when taking for glycerine–water a smaller value of r_s ($r_s = 2\,\mathrm{mm}$) than for FC-72 and water ($r_s = 3\,\mathrm{mm}$). The model of Zeff *et al.* indicates that the cavity collapse is homothetic so that the radius, r_s, of the singularity will be smaller when the cavity aspect ratio is large. In glycerine–water, the cavity aspect ratio is $\ell/r_{ca} \approx 2$, leading to a smaller value of r_s, hence, a larger jet velocity. There is a large dispersion of the jet velocity data because small perturbations may have a large effect. In particular, the conditions at the singularity require very fine-tuning and many trials are necessary to achieve a very high velocity. Zeff *et al.* have only one data point at $60\,\mathrm{m\,s^{-1}}$. We have not reached such a velocity value with about 30 runs. In some experiments, a 1 % ILFORD ILFOTOL in distilled water was used. The photo fluid solution reduces the surface tension to $\sigma \approx 45\,\mathrm{dyn\,cm^{-1}}$, but does not seem to completely eliminate surface rigidity (see the Appendix). Parasitic capillary waves are reduced and the wave crest, because of the larger surface tension compared with FC-72, remains axisymmetric. The cavity that is formed is smaller and of larger aspect ratio than in water or FC-72, hence giving rise to a larger jet velocity.

7. Conclusions

The experimentally determined stability threshold of the parametrically forced axisymmetric gravity wave mode (0,1) in a low viscosity and low kinematic surface tension fluid in a circular cylinder is shown to be in good agreement with the HM theory. Bifurcations to other wave modes, namely modes (2,1) and (3,1), take place at forcing frequencies where the stability thresholds of the different wave modes overlap. Stationary finite-amplitude wave motions exist between the stability threshold and the wave-breaking threshold established in the present experiments. The parametric instability of the axisymmetric mode is shown to be supercritical at the natural frequency and above, and subcritical in a certain frequency range below. Above the instability threshold, the temporal growth of the wave amplitude is exponential after some initial time delay that depends on forcing amplitude with respect to the threshold forcing amplitude. The amplitude response curve shows that near the breaking boundary, the finite-amplitude wave motions exhibit amplitude modulations. These modulations occur on a slow time scale or by period tripling, similar to what has been observed by Jiang *et al.* (1998) for two-dimensional breaking waves. However, here, period tripling occurs without wave breaking or spilling.

In the unstable wave-breaking regime, drop pinch-off at the wave crest occurs or an intense jet may emerge suddenly. This finite-time singularity, demonstrated by Zeff *et al.* (2000) in fluids of high viscosity, is caused by cavity collapse. The cavity is created by the large-amplitude wave crest that falls nearly freely under gravity and surface tension forces and impinges on the wave trough. The present experiments demonstrate that this near singularity is possible in low viscosity and low kinematic surface tension liquids. Using the results of Zeff *et al.* we first developed a Weber-number scaling for the jet velocity that takes into account the container size in addition to the fluid properties. However, the analysis of the results in two containers of different radii and the use of three different liquids indicate that the jet velocity scales on the wave fluid velocity that suggests a Froude-number scaling. Nevertheless, surface tension and especially viscosity (when the Ohnesorge number is of order 1) affect the intensity of the jet by affecting the wave crest shape and hence the cavity aspect ratio.

https://doi.org/10.1017/S0022112008000165 Published online by Cambridge University Press

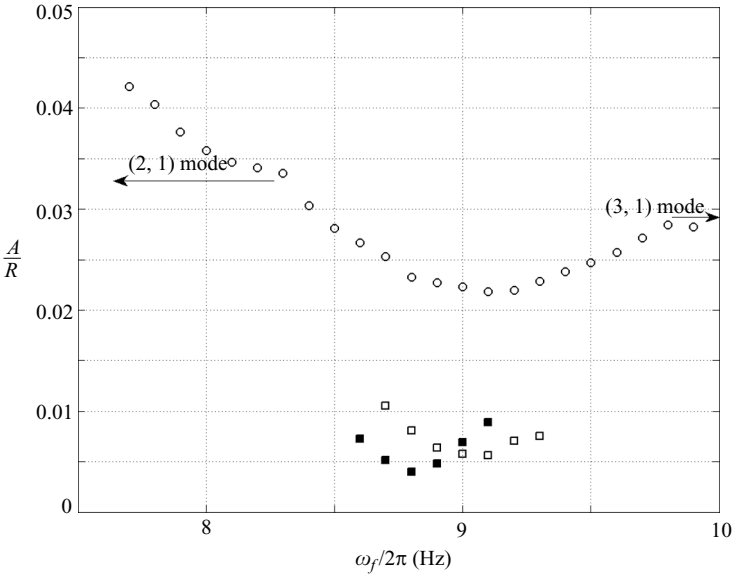


FIGURE 17. Forcing amplitude instability threshold versus forcing frequency; □, distilled water; ■, distilled water with 1 % photo fluid added; ○, glycerine–water. The theoretical natural frequencies (1) of the axisymmetric mode (0,1) are $\omega_{01} = 27.89$ rad s^{-1} for glycerine–water and 27.99 rad s^{-1} for water. For water with photo fluid $\omega_{01} = 27.89$ rad s^{-1} as for glycerine–water (no viscous correction applied). The corresponding forcing frequencies are, respectively, $\omega_f/2\pi \approx 8.88$ and 8.91 Hz.

What happens is that the wave crest, by inertial upward projection, can reach amplitudes of $b \approx R$ that are much larger than the wave amplitude where the downward wave crest acceleration is equal to gravity (plus acceleration due to surface tension), which is about $b \approx 0.3R$. The shape of this wave crest and the adjacent fluid column is affected by surface tension or viscosity when the Ohnesorge number $Oh = \nu/\sqrt{\sigma\, r_1/\rho}$ is of order 1, which is the case for glycerine–water. When the main wave accelerates downward, the fluid column above (above $0.3R$) falls back freely under gravity plus surface tension (effective downward acceleration a_{cr}, table 1) and impinges on the wave trough, forming a cavity. Its radius and depth depend on the wave-crest amplitude and shape and on a_{cr}. The (inertial) collapse of this cavity and jet emergence are then a function of the wave velocity $b\omega \approx \sqrt{gR}$ and of the radius r_s (quasi-singularity) that depends on the cavity aspect ratio ℓ/r_{ca}, determined by surface tension and/or viscosity.

The valuable technical help of Pierre Carecchio, Joseph Virone and François Bonnel is gratefully acknowledged. The work was financially supported by contract CNES 60167 within the COMPERE programme.

Appendix. Stability threshold forcing amplitude for glycerine–water and water

In figure 17, we show the measured forcing amplitude instability threshold as a function of forcing frequency for water and glycerine–water in the $R = 5$ cm container. The observed natural frequencies are nearly identical and are larger $\omega_f/2\pi \cong 9.1$ Hz than the natural frequencies calculated from (1) that would correspond to forcing frequencies $\omega_f/2\pi \cong 8.88$ Hz. This is because the contact line is practically pinned to

https://doi.org/10.1017/S0022112008000165 Published online by Cambridge University Press

the container wall resulting in a higher wave frequency. The effect of contact line conditions on frequency has been pointed out by Benjamin & Scott (1979) in the context of travelling surface waves in a narrow rectangular channel. The speed of wave propagation is increased by the stiffening effect of surface tension with the contact line pinned to the wall. When a 1 % ILFORD ILFOTOL fluid is added to distilled water, the measured frequency is close to the theoretical value.

In glycerine–water, because of its large kinematic viscosity ($\nu \approx 2.5\,\mathrm{cm^2\,s^{-1}}$), damping is expected to be very large. From the measured critical forcing amplitude of $A/R \cong 0.021$ at the natural frequency (figure 17), a damping ratio $\delta \approx 0.081$ is obtained from (6). This corresponds to a decrease in wave amplitude by $1/\mathrm{e}$ in two wave periods. From (2*b*) we obtain $\delta \approx 0.084$ when $C \approx 1$. For water we obtain from figure 17 a value of $\delta \approx 0.019$, whereas from (2*b*) with $C = 1$ we obtain $\delta \approx 0.0053$. This indicates that the free surface has rigidity so that damping at the free surface is important. The parasitic capillary waves in water, observed on the wave crest during jet formation, may be related to this surface rigidity.

When 1 % photo fluid (ILFOD ILFOTOL) is added to water, the damping is somewhat reduced. From figure 17 and (6), the damping is $\delta \approx 0.019$ so that in (2*b*) the constant $C \approx 3.5$. This would indicate that the surface rigidity is only slightly reduced, but the contact line is free to move because the frequency is close to the theoretical value.

REFERENCES

Abramson, H. N. (ed.) 1966 The dynamic behavior of liquids in moving containers. *NASA TR* SP-106.

Benielli, D. & Sommeria, J. L. 1998 Excitation and breaking of internal gravity waves by parametric instability. *J. Fluid Mech.* **374**, 117–144.

Benjamin, T. B. & Scott, J. C. 1979 Gravity–capillary waves with edge constraints. *J. Fluid Mech.* **92**, 241–267.

Benjamin, T. B. & Ursell, F. 1954 The stability of plane free surface of a liquid in a vertical periodic motion. *Proc. R. Soc. Lond.* A **225**, 505–515.

Bredmose, H., Brocchini, M., Peregrine, D. H. & Thais, L. 2003 Experimental investigation and numerical modelling of steep forced water waves. *J. Fluid Mech.* **490**, 217–249.

Dodge, F. T. 1966 Vertical excitation of a propellant tank. In 'I The dynamic behavior of liquids in moving containers', chap. 8 (ed. H. N. Abramson). *NASA TR* SP-106.

Edwards, W. S. & Fauve, S. 1994 Patterns and quasi-patterns in the Faraday experiment. *J. Fluid Mech.* **278**, 123–148.

Faltinsen, O., M., Rognebakke, O. F., Lukovsky, I. A. & Timokha, A. N. 2000 Multidimensional modal analysis of nonlinear sloshing in a rectangular tank with finite water depth. *J. Fluid Mech.* **407**, 201–234.

Faltinsen, O. M., Rognebakke, O. F. & Timokha, A. N. 2003 Resonant three-dimensional nonlinear sloshing in a square-base basin. *J. Fluid Mech.* **487**, 1–42.

Feng, J. C. & Sethna, P. R. 1989 Symmetry-breaking bifurcations in resonant surface waves. *J. Fluid Mech.* **199**, 495–518.

Henderson, D. M. & Miles, J. W. 1990 Single-mode Faraday waves in small cylinders. *J. Fluid Mech.* **213**, 95–109.

Henderson, D. M. & Miles, J. W. 1994 Surface-wave damping in a circular cylinder with a fixed contact line. *J. Fluid Mech.* **275**, 285–299.

Hopfinger, E. J. & Baumbach, V. 2007 Liquid sloshing in cylindrical fuel tanks. *2nd EUCASS Proc. Brussels*, paper 1-04-04.

Ibrahim, R. A. 2005 *Liquid Sloshing Dynamics*. Cambridge University Press.

Jiang, L., Ting, C.-L., Perlin, M. & Schultz, W. W. 1996 Moderate and steep Faraday waves: instabilities, modulation and temporal asymmetries. *J. Fluid Mech.* **329**, 275–307.

https://doi.org/10.1017/S0022112008000165 Published online by Cambridge University Press

Jiang, L., Perlin, M. & Schultz, W. W. 1998 Period tripling and energy dissipation of breaking standing waves. *J. Fluid Mech.* **369**, 273–299.

Kumar, K. & Tuckerman, L. S. 1994 Parametric instability of the interface between two fluids. *J. Fluid Mech.* **279**, 49–68.

Lighthill, J. 1978 *Waves in Fluids.* Cambridge University Press.

Longuet-Higgins, M. S. 1983 On the joint distribution of wave period and amplitudes in a random wave field. *Proc. R. Soc. Lond.* A **389**, 241–258.

Martel, C., Nicolas, J. A. & Vega, J. M. 1998 Surface-wave damping in a brimful circular cylinder. *J. Fluid Mech.* **360**, 213–228.

Miles, J. W. 1984 Resonantly forced surface waves in a circular cylinder. *J. Fluid Mech.* **149**, 15–31.

Miles, J. W. & Henderson, D. M. 1990 Parametrically forced surface waves. *Annu. Rev. Fluid Mech.* **22**, 143–165.

Miles, J. W. & Henderson, D. M. 1998 A note on interior *vs.* boundary-layer damping of surface waves in a circular cylinder. *J. Fluid Mech.* **364**, 319–323.

Milgram, J. H. 1969 The motion of a fluid in a cylindrical container with a free surface following vertical impact. *J. Fluid Mech.* **37**, 453–448.

Nayfeh, A. H. 1987 Surface waves in closed basins under parametric and internal resonances. *Phys. Fluids* **30**, 2976–2983.

Peregrine, D. H., Bredmose, H., McCobe, A., Bullock, G., Obhrai, C., Müller, G. & Wolters, G. 2004 Violent water wave impact on walls and the role of air. *Proc. 29th Intl Conf. Coastal Engng Lisbon* (ed. J. McK. Smith), *World Sci.* **4**, 4005–4017.

Perlin, M. & Schultz, W. 2000 Capillary effects on surface waves. *Annu. Rev. Fluid Mech.* **32**, 241–274.

Royon-Lebeaud, A., Hopfinger, E. J. & Cartellier, A. 2007 Liquid sloshing and wave breaking in circular and square-base cylindrical containers. *J. Fluid Mech.* **577**, 467–494.

Simonelli, F. & Gollub, J. P. 1989 Surface wave mode interactions: effects of symmetry and degeneracy. *J. Fluid Mech.* **199**, 471–494.

Taylor, G. I. 1950 The instability of liquid surfaces when accelerated in the direction perpendicular to their planes. I. *Proc. R. Soc. Lond.* A **201**, 192.

Taylor, G. I. 1953 An experimental study of standing waves. *Proc. R. Soc. Lond.* A **218**, 44–59.

Zeff, B. W., Kleber, B., Fineberg, J. & Lathrop, D. P. 2000 Singularity dynamics in curvature collapse and jet eruption on a fluid surface. *Nature* **403**, 401–404.

https://doi.org/10.1017/S0022112008000165 Published online by Cambridge University Press